

ATOMIC PHYSICS

The helion charge radius from laser spectroscopy of muonic helium-3 ions

Karsten Schuhmann¹, Luis M. P. Fernandes², François Nez³, Marwan Abdou Ahmed⁴, Fernando D. Amaro², Pedro Amaro⁵, François Biraben³, Tzu-Ling Chen⁶, Daniel S. Covita⁷, Andreas J. Dax⁸, Marc Diepold⁹, Beatrice Franke⁹, Sandrine Galtier³, Andrea L. Gouvea², Johannes Götzfried⁹, Thomas Graf⁴, Theodor W. Hänsch^{9,10}, Malte Hildebrandt⁸, Paul Indelicato³, Lucile Julien³, Klaus Kirch^{1,8}, Andreas Knecht⁸, Franz Kottmann^{1,8}, Julian J. Krauth^{9,11}, Yi-Wei Liu⁶, Jorge Machado⁵, Cristina M. B. Monteiro², Françoise Mulhauser⁹, Boris Naar¹, Tobias Nebel⁹, Joaquim M. F. dos Santos², José Paulo Santos⁵, Csilla I. Szabo³, David Taqqu^{1,8}, João F. C. A. Veloso⁷, Andreas Voss⁴, Birgit Weichelt⁴, Aldo Antognini^{1,8*}, Randolph Pohl^{9,11*}, The CREMA Collaboration

Hydrogen-like light muonic ions, in which one negative muon replaces all of the electrons, are extremely sensitive probes of nuclear structure. Using pulsed laser spectroscopy, we have measured three $2S$ - $2P$ transitions in the muonic helium-3 ($\mu^3\text{He}^+$) ion, an ion formed by a negative muon and bare helium-3 nucleus. This allowed us to extract the Lamb shift, the $2P$ fine structure splitting, and the $2S$ -hyperfine splitting in $\mu^3\text{He}^+$. Comparing these measurements with theory, we determined the root-mean-square charge radius of the helion (^3He nucleus) to be $r_h = 1.97007(94)$ fm, in good agreement with the value from elastic electron scattering but a factor 15 more accurate. Our results represent benchmarks for few-nucleon theories and open the way for precision quantum electrodynamics tests in He atoms and ions.

The exceptional simplicity of light atomic systems with one or two electrons, such as H, D, He^+ , or He, coupled with the ability to investigate them through laser spectroscopy, offers an outstanding opportunity to test and advance the theory of atomic energy levels. The exquisite relative precision achieved by current experiments and theory (1, 2), however, requires precise knowledge of the root-mean-square (rms) nuclear charge radii. The extended nuclear charge distribution, which is in leading order parameterized by the rms radius, modifies the Coulomb potential inside the nucleus. This in turn leads to subtle shifts of energy levels on the order of 10^{-9} or smaller in light electronic atoms, highlighting the need for measuring rms radii with a precision better than 10^{-3} . This is currently not matched by elastic electron scattering (3), which has traditionally provided nuclear radii.

Nuclear radii play an increasingly important role in nuclear physics, too. The radius of the ^3He nucleus presented here is expected to improve our understanding of ab initio few-nucleon theory and three-nucleon forces, which have been shown to be crucial for our understanding of nuclei (4–6).

Outstanding sensitivity to nuclear properties such as the charge radius is provided by laser spectroscopy of muonic atoms and ions (7–10), where a single negative muon is orbiting a bare nucleus. This is because the muon mass is 200 times larger than the electron mass, which results in a $200^3 \approx 10^7$ enhanced overlap of the atomic wavefunction with the nucleus. Indeed, the leading-order finite-nuclear-size effect scales with the third power of the (reduced) mass of the orbiting particle. In SI units, this finite size effect reads (1)

$$\Delta E_{\text{FNS}}(n, l) = \frac{2c^4}{3\hbar^2} \frac{(Z\alpha)^4}{n^3} m_r^3 r^2 \delta_{10} \quad (1)$$

where n is the principal quantum number, l the angular momentum, c the speed of light, \hbar the reduced Planck constant, α the fine structure constant, Z the atomic number, m_r the reduced mass, and r the rms charge radius of the nucleus. The Kronecker δ_{10} indicates that only S -state energy levels are affected in leading approximation by the finite size because of their wave function overlap with the nucleus.

Here, we present the measurement of three $2S \rightarrow 2P$ transitions of the muonic helium-3 ion $\mu^3\text{He}^+$ (a two-body ion formed by a negative muon and a bare ^3He nucleus) as shown in Fig. 1, from which we extracted the $2S$ - $2P$ Lamb shift, the $2S$ hyperfine splitting (HFS), and the $2P$ fine splitting. From the Lamb shift, we have then extracted the rms charge radius of the ^3He (helion) nucleus r_h with a relative precision of 7×10^{-4} , improving the previous best value (3) from elastic electron scattering by a factor of 15. From the comparison between $2S$ HFS and theory, we extracted the two-photon-exchange contribution which is the leading-order nuclear structure dependent contribution for the hyperfine splitting.

The $2S$ - $2P$ transition frequencies were measured by pulsed laser spectroscopy at wavelengths around 850 to 940 nm (frequencies of 310 to 350 THz) to an accuracy of ~ 20 GHz corresponding to relative accuracies of ~ 50 ppm. The resonances were exposed by detecting the K_{α} x-ray of 8 keV energy emitted from $2P \rightarrow 1S$ de-excitation after a successful laser transition from the $2S$ to the $2P$ state. The 50-ppm measurement precision has to be compared with the energy shift caused by the finite-size effect (Eq. 1) that contributes as much as 25% to the $2S$ - $2P$ energy splitting due to its $m_r Z^4$ dependence. The binding energy of this hydrogen-like system, scaling as $Z^2 m_r$, is strongly enhanced compared with hydrogen, whereas the atomic size (Bohr radius), scaling as $1/Zm_r$, is strongly reduced, making this atom virtually immune to external perturbation. Because of its $m_r Z^4$ dependence, the decay rate from the $2P$ state is also vastly increased compared with normal atoms, resulting in a $2P$ -linewidth of 319 GHz. This broad linewidth represents by far the main limitation to our experimental precision.

Principle and experimental setup

The experiment was performed at the CHRISP facility at the Paul Scherrer Institute, where $\mu^3\text{He}^+$ ions are formed in highly excited states by stopping a keV-energy muon in a low-pressure (2 mbar) ^3He gas target at room temperature and placed in a 5 T solenoid (Fig. 2). The newly formed $\mu^3\text{He}^+$ ions de-excite to the $1S$ state in a fast (nanosecond-scale) and complex cascade process with a fraction of $\sim 1\%$, reaching the metastable $2S$ state with a lifetime of $\sim 1.7 \mu\text{s}$ at this low target pressure. This lifetime is sufficiently long to enable triggering of our pulsed laser to perform spectroscopy of the $2S$ - $2P$ splitting.

¹Institute for Particle Physics and Astrophysics, ETH Zurich, Zurich, Switzerland. ²LIBPhys, Physics Department, Universidade de Coimbra, Coimbra, Portugal. ³Laboratoire Kastler Brossel, UPMC-Sorbonne Universités, CNRS, ENS-PSL Research University Collège de France, Paris, France. ⁴Institut für Strahlwerkzeuge, Universität Stuttgart, Stuttgart, Germany. ⁵Laboratório de Instrumentação, Engenharia Biomédica e Física da Radiação (LIBPhys-UNL) e Departamento de Física da Faculdade de Ciências e Tecnologia da Universidade Nova de Lisboa, Monte da Caparica, Caparica, Portugal. ⁶Physics Department, National Tsing Hua University, Hsincho, Taiwan. ⁷IN, Universidade de Aveiro, Campus de Santiago, Aveiro, Portugal. ⁸PSI Center for Neutron and Muon Sciences, Villigen PSI, Switzerland. ⁹Max-Planck-Institut für Quantenoptik, Garching, Germany. ¹⁰Faculty of Physics, Ludwig-Maximilian University of Munich, Munich, Germany. ¹¹Johannes Gutenberg University Mainz, Institut für Physik, QUANTUM, & Exzellenzcluster PRISMA+, Mainz, Germany. *Corresponding author. Email: aldo.antognini@psi.ch (A.A.); pohl@uni-mainz.de (R.P.)

To this end, a muon entering the target is detected (7, 11) and triggers a laser system that delivers a pulse to excite the $2S$ into the $2P$ state after a delay of $\sim 1 \mu\text{s}$. The laser pulse is injected into a multipass cell formed by two elongated mirrors that fold the light back and forth to illuminate the elongated muon stopping volume. A successful laser excitation is established by detecting the 8-keV energy K_α x-ray from the $2P$ de-excitation into the ground state. This is accomplished using two rows of large area avalanche photodiodes (LAAPDs) placed above and below the muon stopping volume, respectively, and covering 30% solid angle. The $2S$ - $2P$ resonances are eventually obtained by plotting the number of K_α x-rays detected in time coincidence with the laser light as a function of the laser frequency. For more details on the experiment, see (12).

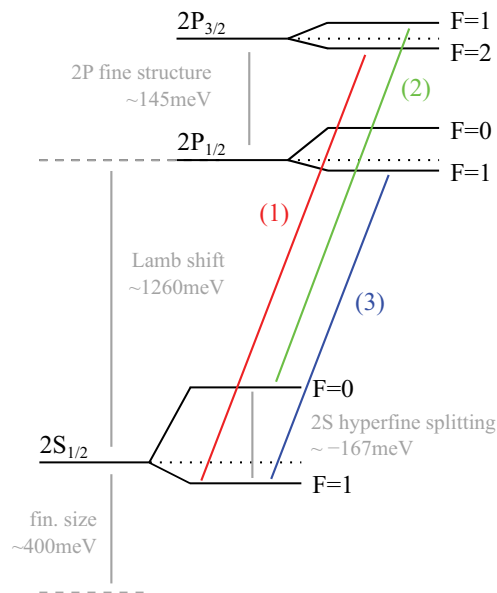


Fig. 1. Energy levels. Shown is the scheme (not to scale) of the $n=2$ energy levels in $\mu^3\text{He}^+$ and the measured transitions. The inverted ordering of the hyperfine levels is caused by the negative magnetic moment of the helion.

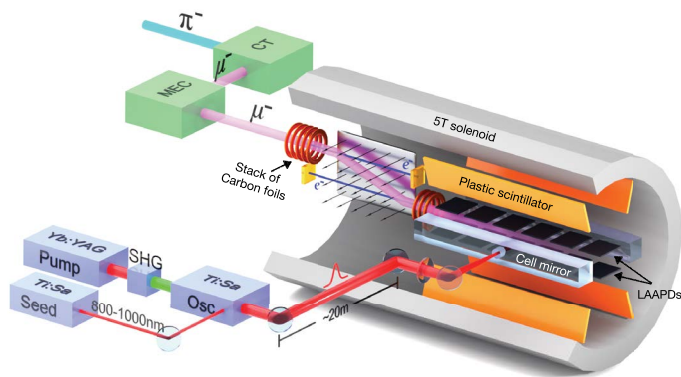


Fig. 2. Sketch of the experimental setup. CT, cyclotron trap; MEC, muon extraction channel; Ti:Sa, titanium-sapphire laser; Yb:YAG thin-disk laser; SHG, second harmonic generation. The arrows indicate the electric field of the $E \times B$ Wien filter. Muons entering the target are detected through the electrons generated in two stacks of carbon foils. The laser pulses are coupled in the multipass cell through a hole in one of the cell mirrors. LAAPDs are placed above and below the muon stopping volume.

Measurements and data analysis

The events used to expose the three $2S$ - $2P$ resonances shown in Fig. 1 had to fulfill the following sequence: a muon is detected in the entrance counter, a K_α x-ray is detected in the LAAPDs in time coincidence with the laser light in the cavity, and a decay electron is detected afterward in the electron counters (or LAAPDs). To obtain the resonances shown in Fig. 3, the number of these events is plotted versus the laser frequency and normalized to the number of prompt K_α x-rays so that variations of the number of muons and x-ray detection efficiency do not affect the results. The laser frequency was alternated on the two sides of the resonance every 1 to 2 hours to reduce a possible distortion of the measured resonance due to variations of the performance of the experimental setup. The injected pulse energy was limited to 5 mJ to minimize saturation effects and optically induced damage of the cavity coating. Because a minimum pulse-to-pulse separation of ~ 2 ms was imposed on the laser system for increased stability, about half of the entering muons did not trigger the laser system. However, these “laser-off events” were used to precisely measure the average background, yielding the yellow bands in Fig. 3.

Transition (1) took ~ 2 weeks of continuous measurement; transitions (2) and (3) were measured together, with ~ 3 weeks of continuous data taking. For the first transition, on resonance, we observed a rate of ~ 7 events/h including a background rate of ~ 2 events/h.

The center frequency of the measured lines was obtained by fitting the data with a line shape model. The model is a Lorentzian that accounts for the laser pulse energy measured for every pulse. It can therefore only be evaluated at the position of each data point. This leads to the distortion in the line shape seen in Fig. 3. From the line shape fit we obtain the following transition frequencies:

$$\nu_{\text{exp}}^{(1)} \equiv \nu(2P_{3/2}^{F=2} - 2S_{1/2}^{F=1}) = 347.212(20)^{\text{stat}}(1)^{\text{sys}} \text{ THz} \quad (2)$$

$$\nu_{\text{exp}}^{(2)} \equiv \nu(2P_{3/2}^{F=1} - 2S_{1/2}^{F=0}) = 312.830(21)^{\text{stat}}(1)^{\text{sys}} \text{ THz} \quad (3)$$

$$\nu_{\text{exp}}^{(3)} \equiv \nu(2P_{1/2}^{F=1} - 2S_{1/2}^{F=1}) = 310.814(20)^{\text{stat}}(1)^{\text{sys}} \text{ THz} \quad (4)$$

The fit was done with a fixed linewidth of $\Gamma = 318.7$ GHz at FWHM, given by the $2P$ decay rate (13, 14). A separate fit with a free width resulted in widths that agreed with the theoretical one. The total uncertainty of about 20 GHz, corresponding to $\sim 6 \times 10^{-2} \Gamma$, is dominated by statistics. The combined systematic uncertainty of each transition frequency is 1 GHz (12).

The measured transition frequencies Eqs. 2 to 4 yield the energy splittings

$$\Delta E_{\text{exp}}^{(1)} = 1435.951(81) \text{ meV} \quad (5)$$

$$\Delta E_{\text{exp}}^{(2)} = 1293.759(86) \text{ meV} \quad (6)$$

$$\Delta E_{\text{exp}}^{(3)} = 1285.425(81) \text{ meV} \quad (7)$$

through the relation $1 \text{ meV} \triangleq 241.798935 \text{ GHz}$. The uncertainties given here are the total experimental uncertainties, which are completely dominated by statistics.

Experimental results

From the three transition measurements between $2S$ and $2P$ states with different fine and hyperfine sublevels, it is possible to determine three quantities: we choose the Lamb shift $E_{\text{LS}} = \Delta E(2P_{1/2} - 2S_{1/2})$, the $2S$ hyperfine splitting E_{HFS} , and the $2P$ fine splitting $E_{\text{FS}} = \Delta E(2P_{3/2}$

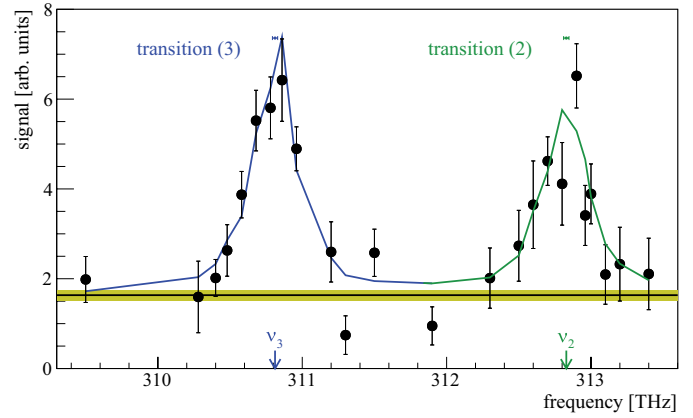
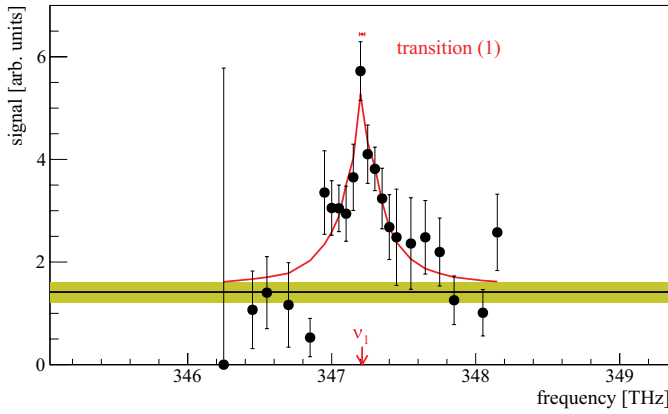


Fig. 3. Measured $2S \rightarrow 2P$ transitions in $\mu^3\text{He}^+$. The black data points show the number of laser-induced K_α x-ray events normalized to prompt K_α events. The data are fitted with a line shape model detailed in the main text. This model applies only at the measured points, and the colored lines only connect the fit points. The fitted center frequencies including their uncertainties are indicated by the colored points with error bar above the resonances. The yellow bands indicate the average $\pm 1\sigma$ backgrounds obtained from events where the laser was not fired.

$-2P_{1/2}$). The relations between the measured transition energies and these quantities are given by (12):

$$\Delta E_{\text{exp}}^{(1)} = E_{\text{LS}} - \frac{1}{4}E_{\text{HFS}} + E_{\text{FS}} - 9.23945(26) \text{ meV} \quad (8)$$

$$\Delta E_{\text{exp}}^{(2)} = E_{\text{LS}} + \frac{3}{4}E_{\text{HFS}} + E_{\text{FS}} + 15.05305(44) \text{ meV} \quad (9)$$

$$\Delta E_{\text{exp}}^{(3)} = E_{\text{LS}} - \frac{1}{4}E_{\text{HFS}} - 14.80851(18) \text{ meV} \quad (10)$$

where $E_{\text{HFS}} < 0$ and the numerical values of the last terms in Eqs. 8 to 10 arise from the $2P$ fine and hyperfine splittings, and include the contribution from the mixing of the $F = 1$ levels. These contributions can be calculated with great precision because the $2P$ wave function of the hydrogen-like muonic He ion has negligible overlap with the nucleus, resulting in negligible contributions from nuclear size and structure corrections.

The two most recent theory papers (15, 16) used different conventions for the definition of the $2P_{1/2}$ and $2P_{3/2}$ centroids, which results in differing definitions of the Lamb shift. To obtain the constant terms in Eqs. 8 to 10, we have used the $2P$ levels calculated in (15) and modified them to account for the different definitions (12) such that our final result for the Lamb shift follows the convention of (16).

We can solve the system of equations to obtain the experimental values of the Lamb shift, the $2S$ HFS and the $2P$ fine splitting:

$$E_{\text{LS}}^{\text{exp}} = 1258.612(86) \text{ meV} \quad (11)$$

$$E_{\text{HFS}}^{\text{exp}} = -166.485(118) \text{ meV} \quad (12)$$

$$E_{\text{FS}}^{\text{exp}} = 144.958(114) \text{ meV} \quad (13)$$

The experimental value of the fine splitting $E_{\text{FS}}^{\text{exp}}$ is in excellent agreement with predictions $E_{\text{FS}}^{\text{theo}} = 144.979(5) \text{ meV}$ (15), demonstrating consistency between our three muonic transitions measurements, as well as the correctness of the theory of the $2P$ fine structure. Because of its much smaller uncertainty and consistency with measurements, we

can use the theory value of the fine splitting to solve the system of equations Eqs. 8 to 10 to obtain improved values of the Lamb shift and $2S$ HFS

$$E_{\text{LS}}^{\text{exp}} = 1258.598(48)^{\text{exp}}(3)^{\text{theo}} \text{ meV} \quad (14)$$

$$E_{\text{HFS}}^{\text{exp}} = -166.496(104)^{\text{exp}}(3)^{\text{theo}} \text{ meV} \quad (15)$$

The theoretical uncertainties are from the $\pm 0.005 \text{ meV}$ estimated higher-order corrections to the fine structure in (15), which affects only two of the three measured transitions.

The helion charge radius and the isotope shift

The theory prediction of the Lamb shift has been recently updated accounting for the contributions of various groups. It reads (16):

$$E_{\text{LS}}^{\text{theo}}(r_h^2) = 1644.348(8) \text{ meV} - 103.383(1) r_h^2 \text{ meV/fm}^2 + E_{\text{LS}}^{\text{nucul.struct.}} \quad (16)$$

where the first term accounts for all quantum electrodynamics (QED) corrections independently of the nuclear structure, and the term proportional to r_h^2 accounts for the finite-size correction including radiative corrections to it. The last term

$$E_{\text{LS}}^{\text{nucul.struct.}} = 15.499(378) \text{ meV} \quad (17)$$

is the sum of nuclear structure dependent contributions (17–19) which is dominated by the nuclear two- and three-photon exchange contributions (2PE and 3PE, respectively). Here, the 2PE amounts to 16.38(31) meV, of which 0.647(55) meV is from the individual nucleons. The full 3PE has not been calculated explicitly, and we use the conventional scaling from the calculated elastic 3PE (10, 19). Comparing this theory prediction with the measured Lamb shift $E_{\text{LS}}^{\text{exp}}$, we obtain the rms charge radius of the helion

$$r_h = 1.97007(12)^{\text{exp}}(93)^{\text{theo}} \text{ fm} = 1.97007(94) \text{ fm} \quad (18)$$

This value is 15 times more precise than the previous best value from elastic electron- ^3He scattering of 1.973(14) fm (3) and consistent with it (Fig. 4).

Our value could be further improved by almost an order of magnitude by advancing the calculations leading to Eq. 17, both for the nucleus and the nucleons (16, 18, 20).

It is interesting to compare this value with the helion charge radius as obtained from most recent nuclear theories, which uses chiral effective field theory to describe the nuclear interaction and ab initio

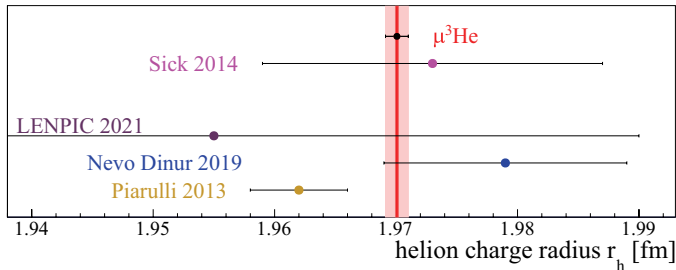


Fig. 4. Recent determinations of the ${}^3\text{He}$ nucleus (helion) charge radius. The dark and light bands indicate the experimental and total uncertainty in our measurement. The value of Sick of 1.973(14) fm (3) is from the world data on elastic electron scattering. The other values are recent predictions from nuclear few-body theory: Piarulli and colleagues, 1.962(4) fm (21,22); Nevo Dinur *et al.*, 1.979(10) fm (50); and the LENPIC collaboration, 1.955(34) fm (24,25). The latter value was obtained using the point-proton structure radius and procedure explained in (24).

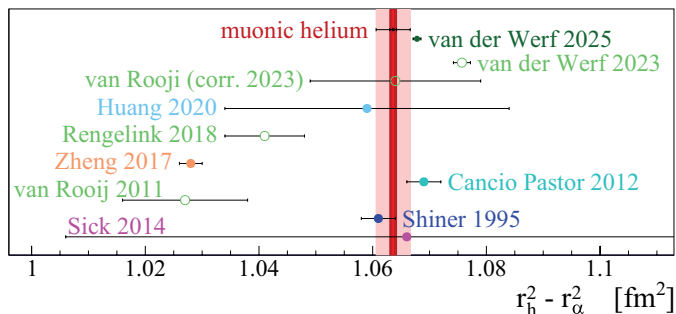


Fig. 5. Squared charge radius difference $r_h^2 - r_\alpha^2$. The isotope shift in ordinary He atoms (2, 27–32, 34) is compared to our value from muonic ions. The dark and light bands indicate the experimental and total uncertainty of our determination. The values of Shiner *et al.* (27) and Cancio Pastor *et al.* (29) have been corrected for improved theory calculations (26) but may lack a systematic correction associated with quantum interference effects (55), as suggested in (35). The value of Zheng *et al.* (31) may have to be corrected for a systematic Doppler shift (36). The most recent work from Amsterdam by van der Werf (2) supersedes the results from van Rooij (28) and Rengeling (32) and gives an updated result of (28). Good agreement is found when the hyperfine mixing in ordinary helium (37,38) is accounted for in van der Werf *et al.* (2). Another precise value is soon expected from the ionization energy in metastable helium (51).

methods to solve the quantum-mechanical few-body problem. Figure 4 shows some of the most recent results taken from (21–25) depicting an overall satisfactory agreement between the measured value and the various predictions and highlighting the role of the helion charge radius as a benchmark for precision nuclear theory.

Spectroscopy of ordinary helium atoms cannot yet provide precise values of the helion and alpha-particle charge radii given the present uncertainty of the three-body atomic theory. However, in the isotope shift, several cancellations take place in the theory (26) of the energy levels so that an accurate determination of the squared charge radius difference $r_h^2 - r_\alpha^2$ is possible (27–32) (Fig. 5). Here, r_α is the alpha particle (${}^4\text{He}$) charge radius. The scattering of the values obtained so far shown in Fig. 5, however, reveals some tensions that highlight the challenges faced by both theory and experiments.

It is therefore interesting to address this quantity by considering the isotope shift in muonic helium ions (16, 33)

$$r_h^2 - r_\alpha^2 = -\frac{E_{\text{LS}}^{\text{exp}}({}^3\text{He}^+)}{103.383 \frac{\text{meV}}{\text{fm}^2}} + \frac{E_{\text{LS}}^{\text{exp}}({}^4\text{He}^+)}{106.209 \frac{\text{meV}}{\text{fm}^2}} + 0.2585(30) \text{ fm}^2 \quad (19)$$

where the last term is calculated taking advantage of some cancellations of nucleon and nuclear structure contributions in $E_{\text{LS}}^{\text{nucl.struct.}}$. Inserting the measured $\mu^4\text{He}^+$ Lamb shift (10) of $E_{\text{LS}}^{\text{exp}}({}^4\text{He}^+) = 1378.521(48) \text{ meV}$ and $E_{\text{LS}}^{\text{exp}}({}^3\text{He}^+)$ from Eq. 11 into this expression, we obtain

$$r_h^2 - r_\alpha^2 = 1.0636(6)^{\text{exp}}(30)^{\text{theo}} \text{ fm}^2 \quad (20)$$

where the theory uncertainty is dominated by the nuclear 2PE. The value in Eq. 20 can be compared with various isotope shift measurements obtained in regular He atoms with two electrons (27–32, 34), where long-standing discrepancies exist (Fig. 4). Several systematic shifts were recently identified in these measurements (2, 35, 36). Initially, our result deviated by 3.6σ from the most recent and most precise value by the Amsterdam group (2). However, recent calculations of the hyperfine mixing in ordinary helium (37, 38) brought the Amsterdam value in agreement with our result.

Our measurements in muonic helium ions do not require the exquisite experimental accuracy of 10^{-12} reached in ordinary helium atoms and are not sensitive to systematic effects. Conversely, our results are limited by the nuclear structure effects of $E_{\text{LS}}^{\text{nucl.struct.}}$, which are much larger in muonic systems (18, 23, 39–42).

For completeness, we quote here the updated Lamb shift theory in $\mu^4\text{He}^+$ from (16)

$$E_{\text{LS}}^{\text{theo}}(r_\alpha^2) = 1668.491(7) \text{ meV} - 106.209 r_\alpha^2 \text{ meV/fm}^2 + 9.276(433) \text{ meV} \quad (21)$$

Combined with the Lamb shift in $\mu^4\text{He}^+$ that we have measured in (10), this yields an updated ${}^4\text{He}$ charge radius of $r_\alpha = 1.6786(12) \text{ fm}$ with a 45% larger uncertainty compared with our previous determination, which used the theory summarized in (33). The new r_α was obtained using the 2PE contribution calculated solely from ab initio theory (18), whereas previously, we split it into a third-Zemach moment (Friar radius) contribution obtained from electron elastic scattering and a polarizability contribution from few-nucleon theories (18). Because this splitting could lead to some inconsistencies (16), we now opt for the solution fully based on few-body theories (18).

Nuclear-structure contribution for the 2S HFS

By comparing the measured 2S HFS $E_{\text{HFS}}^{\text{exp}}$ in $\mu^3\text{He}^+$ with the corresponding theory prediction (43)

$$E_{\text{HFS}}^{\text{theo}} = -172.7457(89) \text{ meV} + E_{\text{HFS}}^{\text{nucl.struct.}} \quad (22)$$

we extract the nuclear structure-dependent contributions (2PE and higher orders) to the 2S hyperfine splitting

$$E_{\text{HFS}}^{\text{nucl.struct.}} = 6.25(10) \text{ meV} \quad (23)$$

with an uncertainty arising almost entirely from the statistical uncertainties of our measurements. Subtracting from $E_{\text{HFS}}^{\text{nucl.struct.}}$ the elastic part of the two-photon-exchange contribution $\Delta E_{2\text{PE}}^{\text{Zemach}} = 2.5836 \text{ meV/fm}$ $r_Z = 6.53(4) \text{ meV}$, where $r_Z = 2.528(16) \text{ fm}$ is the Zemach radius of the ${}^3\text{He}$ nucleus (3, 23), we can obtain a value for the hitherto unknown polarizability contribution to the 2S hyperfine splitting of $-0.28(10) \text{ meV}$ (that includes also higher-order contributions). This represents an important benchmark to refine our understanding of the magnetic structure of the ${}^3\text{He}$ nucleus. It also allows us, using appropriate scaling, to predict the nuclear structure contribution of the ground-state hyperfine splitting in $\mu^3\text{He}^+$, restricting considerably the range where we can search for this resonance.

Discussion and outlook

Laser spectroscopy of $\mu^3\text{He}^+$ and $\mu^4\text{He}^+$ (10) ions provides precision values of ${}^3\text{He}$ and ${}^4\text{He}$ charge radii and the isotope shift (Eq. 20). These are low-energy observables for ab initio nuclear structure theory, complementing nuclear binding energies and magnetic moments.

They can serve as benchmarks for few-body calculations and the systematic development of the many-body nuclear potential and electromagnetic currents used in these calculations (4, 21–23, 44–46).

In the near future, measurements in ordinary He^+ (47, 48), together with the radii presented here, can be used to test the QED theory for H-like two-body systems (20, 49), with particular sensitivity to higher-order corrections that scale with high powers of $(Z\alpha)^{5\dots 8}$.

Eventually, these measurements in ordinary He^+ may determine the nuclear charge radii with even better accuracy than the ones given here. In muonic atoms, the nuclear structure effects (2PE and 3PE) are enhanced by (at least) another power of the lepton mass relative to the finite-size effect. They are thus the main source of uncertainty for the radii from muonic atoms (Eq. 16) but play a small role in electronic atoms (49). Such a precise charge radius from electronic atoms, combined with Eqs. 11 and 16, will then yield $E_{\text{LS}}^{\text{nucl.struct.}}$ from experiment, providing an improved benchmark for nuclear structure calculations (18, 39, 41, 42, 50).

The charge radii from muonic ions are also essential for comparing measurements (2, 27–32, 34, 51) and theory in the neutral He atoms, which have experienced notable advances in recent years (52). This ultimately opens the way for precision testing of the challenging three-body QED with two electrons and an independent determination of the Rydberg constant from systems with $Z = 2$.

Finally, comparison of results from electronic (2) and muonic systems can be used to search for physics beyond the Standard Model (53, 54).

REFERENCES AND NOTES

1. E. Tiesinga, P. J. Mohr, D. B. Newell, B. N. Taylor, *Rev. Mod. Phys.* **93**, 025010 (2021).
2. Y. van der Werf, K. Steinebach, R. Jannin, H. L. Bethlehem, K. S. E. Eikema, *Science* **388**, 850–853 (2025).
3. I. Sick, *Phys. Rev. C* **90**, 064002 (2014).
4. H.-W. Hammer, S. König, U. van Kolck, *Rev. Mod. Phys.* **92**, 025004 (2020).
5. E. Epelbaum *et al.*, *Phys. Rev. C* **66**, 064001 (2002).
6. E. Epelbaum, H. Krebs, P. Reinert, *Front. Phys.* **8**, 98 (2020).
7. R. Pohl *et al.*, *Nature* **466**, 213–216 (2010).
8. A. Antognini *et al.*, *Science* **339**, 417–420 (2013).
9. R. Pohl *et al.*, *Science* **353**, 669–673 (2016).
10. J. J. Krauth *et al.*, *Nature* **589**, 527–531 (2021).
11. M. Mühlbauer *et al.*, *Hyp. Interact.* **119**, 305–310 (1999).
12. See the supplementary materials.
13. P. Amaro *et al.*, *Phys. Rev. A* **92**, 022514 (2015).
14. P. Amaro *et al.*, *SciPost Phys.* **13**, 020 (2022).
15. S. G. Karshenboim, E. Y. Korzinin, V. A. Shelyuto, V. G. Ivanov, *Phys. Rev. A* **96**, 022505 (2017).
16. K. Pachucki *et al.*, *Rev. Mod. Phys.* **96**, 015001 (2024).
17. C. E. Carlson, M. Gorchtein, M. Vanderhaeghen, *Phys. Rev. A* **95**, 012506 (2017).
18. C. Ji, S. Bacca, N. Barnea, O. J. Hernandez, N. Nevo Dinur, *J. Phys. G Nucl. Part. Phys.* **45**, 093002 (2018).
19. K. Pachucki, V. Patkóš, V. A. Yerokhin, *Phys. Rev. A* **97**, 062511 (2018).
20. A. Antognini, F. Hagelstein, V. Pascalutsa, *Annu. Rev. Nucl. Part. Sci.* **72**, 389–418 (2022).
21. L. E. Marcucci *et al.*, *J. Phys. G Nucl. Part. Phys.* **43**, 023002 (2016).
22. M. Piarulli *et al.*, *Phys. Rev. C* **87**, 014006 (2013).
23. N. Nevo Dinur *et al.*, *Phys. Rev. C* **99**, 034004 (2019).
24. P. Maris *et al.*, *Phys. Rev. C* **103**, 054001 (2021).
25. P. Maris *et al.*, *Phys. Rev. C* **106**, 064002 (2022).
26. K. Pachucki, V. A. Yerokhin, *Phys. Rev. A* **95**, 062510 (2017).
27. D. Shiner, R. Dixon, V. Vedantham, *Phys. Rev. Lett.* **74**, 3553–3556 (1995).
28. R. van Rooij *et al.*, *Science* **333**, 196–198 (2011).
29. P. Cancio Pastor *et al.*, *Phys. Rev. Lett.* **108**, 143001 (2012).
30. V. Patkóš, V. A. Yerokhin, K. Pachucki, *Phys. Rev. A* **94**, 052508 (2016).
31. X. Zheng *et al.*, *Phys. Rev. Lett.* **119**, 263002 (2017).

32. R. J. Rengelink *et al.*, *Nat. Phys.* **14**, 1132 (2018).
33. M. Diepold *et al.*, *Ann. Phys.* **396**, 220–244 (2018).
34. Y.-J. Huang, Y.-C. Guan, J.-L. Peng, J.-T. Shy, L.-B. Wang, *Phys. Rev. A* **101**, 062507 (2020).
35. A. Marsman, E. A. Hessels, M. Horbatsch, *Phys. Rev. A* **89**, 043403 (2014).
36. J.-L. Wen *et al.*, *Phys. Rev. A* **107**, 042811 (2023).
37. X.-Q. Qi *et al.*, arXiv:2409.09279 [physics.atom-ph] (2024).
38. K. Pachucki, V. Patkóš, V. A. Yerokhin, arXiv:2411.05621 [physics.atom-ph] (2024).
39. O. J. Hernandez, C. Ji, S. Bacca, N. Barnea, *Phys. Rev. C* **100**, 064315 (2019).
40. A. A. Filin *et al.*, *Phys. Rev. C* **103**, 024313 (2021).
41. B. Acharya, S. Bacca, F. Bonaiti, S. S. Li Muli, J. E. Sobczyk, arXiv:2210.04632 [nucl-th] (2022).
42. S. S. Li Muli, B. Acharya, O. J. Hernandez, S. Bacca, *J. Phys. G* **49**, 105101 (2022).
43. B. Franke *et al.*, *Eur. Phys. J. D* **71**, 341 (2017).
44. A. Ekström *et al.*, *Phys. Rev. C* **91**, 051301 (2015).
45. J. E. Lynn *et al.*, *Phys. Rev. C* **96**, 054007 (2017).
46. J. Vanasse, *Phys. Rev. C* **98**, 034003 (2018).
47. J. Moreno *et al.*, *Eur. Phys. J. D* **77**, 67 (2023).
48. E. L. Gründeman *et al.*, *Commun. Phys.* **7**, 414 (2024).
49. S. G. Karshenboim, A. Ozawa, V. A. Shelyuto, R. Szafron, V. G. Ivanov, *Phys. Lett. B* **795**, 432–437 (2019).
50. N. Nevo Dinur *et al.*, *Phys. Rev. C* **99**, 034004 (2019).
51. G. Clausen *et al.*, *Phys. Rev. Lett.* **127**, 093001 (2021).
52. V. Patkóš, V. A. Yerokhin, K. Pachucki, *Phys. Rev. A* **103**, 042809 (2021).
53. C. Frugiele, C. Peset, *J. High Energy Phys.* **2022**, 2 (2022).
54. Y. V. Stadnik, *Phys. Rev. Lett.* **131**, 011001 (2023).
55. R. C. Brown *et al.*, *Phys. Rev. A* **87**, 032504 (2013).
56. K. Schuhmann *et al.*, The helion charge radius from laser spectroscopy of muonic helium-3 ions (OpenScience Project, 2025); <https://doi.org/10.25358/openscience-11269>.

ACKNOWLEDGMENTS

This paper is dedicated to I. Sick and W. Vassen. We thank S. Bacca, N. Barnea, K. Eikema, E. Epelbaum, F. Hagelstein, S. Karshenboim, S. Li Muli, V. Lensky, L. Marcucci, U. Meißner, K. Pachucki, L. Simons, and K. Steinebach for fruitful discussions. **Funding:** This work was supported by the European Research Council (ERC StG grant 279765 and CoG grant 725039); the Deutsche Forschungsgemeinschaft (DFG, German Research Foundation) under Germany's Excellence Strategy EXC PRISMA+ (grant 390831469); European Union's Horizon 2020 research and innovation program (grant STRONG 2020 824093); FEDER and FCT (project PTDC/FIS-NUC/0843/2012; FCT grants SFRH/BPD/76842/2011, SFRH/BPD/92329/2013, and SFRH/BD/52332/2013; and grant DFG GR_3172/9-1); the Swiss National Science Foundation (SNSF grants 138175, 159755, 165854, 197052); and the ETH Femtosecond and Attosecond Science and Technology (ETH-FAST) initiatives as part of the NCCR MUST program. **Author contributions:** K.S., M.A.A., F.B., T.-L.C., A.D., M.D., S.G., T.G., T.W.H., L.J., K.K., F.K., J.J.K., Y.-W.L., B.N., F.N., D.T., J.F.C.A.V., A.V., B.W., A.A., and R.P. designed, built, and operated parts of the laser system. K.S., L.M.P.F., F.D.A., M.D., B.F., A.L.G., M.H., K.K., A.K., F.K., J.J.K., Y.-W.L., J.M., C.M.B.M., F.M., T.N., F.N., J.M.F.S., J.P.S., D.T., J.F.C.A.V., A.A., and R.P. planned, built, and set up the various detectors of the experiment. K.S., F.D.A., P.A., D.S.C., M.D., L.M.P.F., B.F., J.G., J.H., M.H., K.K., A.K., F.K., J.J.K., J.M., F.M., J.P.S., C.I.S., D.T., A.A., and R.P. designed, built, set up, and operated the muon beam line. K.S., F.D.A., M.D., L.M.P.F., B.F., A.K., F.K., J.J.K., J.M., C.M.B.M., F.M., F.N., J.M.F.S., D.T., A.A., and R.P. designed and implemented the electronics used in the experiment. P.A., M.D., A.K., J.J.K., J.P.S., J.V., R.P., and A.A. set up the computing infrastructure, wrote software, and realized the data acquisition system. K.S., F.D.A., P.A., D.S.C., A.J.D., M.D., L.M.P.F., B.F., S.G., J.G., A.L.G., P.I., L.J., A.K., F.K., J.J.K., Y.-W.L., J.M., C.M.B.M., B.N., F.N., J.M.F.S., J.P.S., C.I.S., D.T., J.F.C.A.V., A.A., and R.P. took part in the months-long data-taking runs. P.A., M.D., B.F., P.I., F.K., J.J.K., J.P.S., D.T., A.A., and R.P. did work on theory. K.S., M.D., L.M.P.F., P.I., F.K., J.J.K., C.M.B.M., F.N., J.M.F.S., A.A., and R.P. analyzed the data. J.J.K., F.K., A.A., and R.P. drafted this manuscript. All authors read, edited, and accepted the final version of the manuscript. **Competing interests:** The authors declare no competing interests. **Data and materials availability:** Data and analysis software can be accessed through the OpenScience Project (56). **License information:** Copyright © 2025 the authors, some rights reserved; exclusive licensee American Association for the Advancement of Science. No claim to original US government works. <https://www.science.org/about/science-licenses-journal-article-reuse>.

SUPPLEMENTARY MATERIALS

science.org/doi/10.1126/science.adj2610
Materials and Methods; Supplementary Text; Table S1; References (57–63)
Submitted 15 June 2023; accepted 31 March 2025

[10.1126/science.adj2610](https://science.org/doi/10.1126/science.adj2610)